**THE EUROPEAN
PHYSICAL JOURNAL PLUS**

Numerical investigation of acoustic streaming vortex and operating parameters in curved microchannel: driven by standing surface acoustic wave

Mehrshad Rezadoost Dezfuli, Azadeh Shahidian[a]

Mechanical Engineering Department, K. N. Toosi University of Technology, Tehran, Iran

Abstract The employment of ultrasonic fields to control particles has been received attention for its efficient role in harmless applications such as separation, sorting, and trapping. The capability of this technology in related applications is improved by better analyzing and visualizing the interfacing parameters. In this research, the operating parameters, including working frequency, phase difference, displacement amplitude, cross section, and microchannel material in a water-filled microchannel actuated by standing surface acoustic wave, are studied. Perturbation theory is employed to derive the first-order acoustic field and time-averaged second-order governing equations. Also, appropriate and lately introduced boundary conditions are precisely applied to capture the fluid flow and particle motion. Results show the half-wave resonance model in Pyrex wall can effectively sort particles in regions where Acoustic Streaming (AS) is not disruptive. The new design of the microchannel introduces a different pattern in polystyrene aggregation, which can be applied for further acoustic sorting and separation. Additionally, by increasing frequency in Pyrex, stronger streaming is inclined close to the walls which can be applied to mix sheath flows with the buffer flows in cell lysis application. Comparison of different cross sections for different material at different frequencies significantly help to find a trade-off between Acoustic Radiation Force (ARF) and AS. Operating parameters effect on the AS and ARF is visualized and compared to reveal each case potential for sorting, separation, trapping, and mixing application. This quantitative simulation will help researchers choose the appropriate material and correct resonance frequency for lateral biological applications.

1 Introduction

The rapid growth of lab-on-a-chip systems made sharp progress in standard operations such as sample preparation, sample injection, and sample manipulation [1–4]. Different passive (e.g., deterministic lateral displacement, hydrodynamic filtration, and pinched flow fractionation) and active (e.g., magnetophoresis, dielectrophoresis, and acoustophoresis) techniques are applied to separate particles efficiently in the microchannel [5]. As a label-free and harmless approach showing good bio-compatibility, the acoustic field is utilized to separate bio-cells [6]. There are two actuation methods, including bulk acoustic wave (BAW)[7] and surface acoustic wave (SAW) [8] in acoustofluidic [9] systems. The separation of bio-particles in microfluidic systems has been studied numerically and experimentally in the last few years. Since the early 21st century, microfluidic separation of the particle using BAW has been studied experimentally [10–12]. Successful advents of BAW microchips intrigued researchers to develop this field and utilize SAW microdevices for more efficient sample manipulation [13–16].

Primary numerical investigation on BAW-driven microdevices were focused on the rectangular channel [17, 18]. Later, considering surrounding medium instead of imposing boundary condition [19] and thermal effect [20] is considered to improve the accuracy of results. [21]. The conventional BAW biochips are mostly suffering from high Acoustic Streaming(AS) velocity interfering with the separation [22]. To overcome this challenge, a curved channel is introduced for efficient handling of the sample [23]. Other researchers have extended the investigations from rectangular channels to circular microchannels [24, 25] to introduce new systems. To overcome BAW microchip drawbacks and to enhance the capabilities of acoustofluidic devices, several numerical models represented particle motion and acoustic streaming in SAW actuated devices [26–28]. Further analyses have been conducted toward full modeling and three dimensional analysis of SAW device [29–31]. While considering complete modeling enhances the reliability, imposing boundary conditions can provide satisfactory results [32]. Recently, a three-dimensional model of acoustic radiation force to capture spherical particle agglomeration induced by BAW is numerically investigated and experimentally observed [33]. In this study, different boundary conditions have been applied to capture the behaviors of particle clusters. Contrary to BAW microsystems, analyses on optimizing the channel for better manipulating particles in SAW systems have not been well noticed. This reflects the importance of novel design to overcome streaming interference in particle manipulation and also introducing different type of

---

[a] e-mail: Shahidian@kntu.ac.ir (corresponding author)

material and geometry. Toward this goal, new piezoelectric and wall material has been introduced. Gallium Nitride films with higher input power and thermal stability compared to the conventional Lithium Niobate manipulated micro-particle successfully [34]. In other design examples, polymeric microchips as a whole-structure on resonance with low-cost of manufacturing and high separation efficiency have been continuously designed [35, 36].

Addition to the literature gaps necessity to present novel design and materials, two distinct behavior between SAW-based and BAW-based microchannel make introducing new materials [37] more critical for SAW devices. Because in BAW-micro devices, the surrounding medium is totally on resonance, the pressure anti-node is precisely on the wall and there is no decaying behavior from bottom of the channel to the top of the channel. Hence, the pressure field is uniform across height of the channel. Unlike this behavior, in SAW-micro devices, the Acoustic Radiation Force (ARF) is stronger in bottom of the channel than top of the channel. This feature is unfavorable because on the bottom of channel, acoustic streaming is dominant and it is disruptive to the particle sorting. Also, The SAW-based devices suffer from lack of precisely setting pressure anti-node on the side wall due to the high energy dissipation of PDMS.

In the recent investigations by Devendran et al [38], the importance of height and different actuation method is investigated. It is shown that variation in the excitation method by inducing a traveling wave rather standing wave can mitigate the streaming effect. This method is very sensible to the width of domain and it can exclusively be potential for narrow channels where it is fully influenced by diffractive effect. Also, in this method particles immigrate to the corner of the channels where they are exposed to clogging. To separate Cancer cells from blood [15], a hybrid model is adopted. To increase, the acoustic energy density within the microchannel a piece of pyrex is stuck to the top wall of the microchannel to stop decaying energy of incoming wave. Also, successful sorting of particles [39–41], efforts have been put to separate sensible particles such as nanoscale particles or particles with similar physical properties [14]. Considering recent researches, the interplay of ARF and AS has been converted to trade-off between ARF and AS. One approach to find a balanced design is to investigate the operating parameters.

This research examines the trade-off between ARF and AS for better design by investigation different materials and operating parameters. Even though several numerical research has been conducted on the acoustophoretic motion [42]; however, they have been limited to the study of polystyrene particle motion and fluid behavior in PDMS rectangular microchannels. Experimental investigation in combination with numerical simulation of reduced-fluid modeling [32] of polystyrene particle also helps the society to understand streaming vortices physics finer while it is also limited to a simplified model of a PDMS rectangular microchannel. Rectangular microchannel has been proved to have some potential benefits on particle separation, but curved microchannels have been received very little attention. PDMS as transparent material is widely used in SAW-microfluidic chips, whereas it absorbs acoustic energy and ultimately the separation efficiency. Other materials such as Pyrex can replace PDMS while reflecting the energy to the channel. This study aims to cite potentials of novel design and help experimental researchers to exploit them. Main parameters including frequency, microchannel material, operating phase, cross section, and displacement amplitude are subjected to scrutiny. Investigating all effective operating parameters and comparing them with each other provides a powerful vision for scientists to design effective sorting devices. This scrutiny reveals that when half-wavelength matches the channel width for the Pyrex material, the strength of radiation force increases, and polystyrene moves to the pressure node without sensing the wall effect and acoustic streaming dominance. Furthermore, cross-section effect at different frequencies has been examined. Depending on the manipulation application PDMS and Pyrex can provide different options based on their response to cross-section variance. Investigation of fluid behavior in the circular channel and hard material microchannel could be helpful to researchers to provide a practical alternative design to the problem of cancer cell separation from blood cells.

In this research, firstly, we introduce the computational model and 2-D geometry. Secondly, we employ the perturbation method to derive the governing equations. In the next step, Acoustic field and laminar flow for PDMS and Pyrex wall, trajectories of polystyrene beads in different sizes, and displacement amplitude effect on nonlinear phenomena are discussed.

2 Proposed model

Here the studied domain is described, and material properties are introduced. In the next step, the governing equations and appropriate boundary conditions are explained in detail.

2.1 Computational domain

Typical standing SAW (SSAW) microdevices consist of at least four different domains. These domains include the collection of interdigital transducers (IDTs) and piezoelectric substrate, fluid domain, and microchannel. Because solving all the physics simultaneously increases the numerical cost sharply, the simulation is simplified to the fluid domain, and the impact of other physics is imposed as boundary conditions. As a result, our computational domain reduces to a semicircular microchannel with a radius of 75 micrometers. In Fig. 1, the three-dimensional sketch of the separator device is shown. The 2D cross-section purple plane (perpendicular to fluid flow) is the computational model that represents the acoustic influence on fluid behavior. This research study Pyrex microchannel with a working frequency of 13.313 MHz. Further changes in operating parameters are applied in other sections, and their effect on acoustic field and laminar flow are discussed.

Fig. 1 Three-dimensional sketch of semicircular microchannel actuated by two counter-propagating interdigital transducers (IDT)
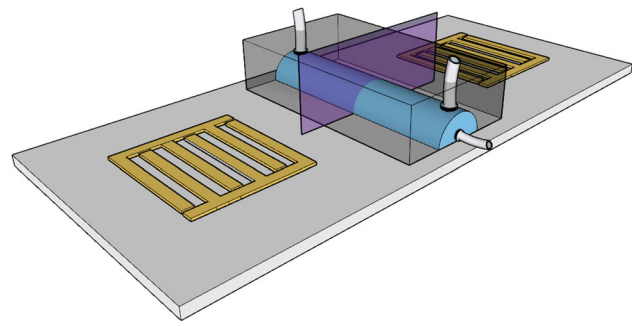

Table 1 Materials and properties

Water	Symbol	Value
Density[a]	ρ_f	997 kg m^{-3}
Speed of sound[b]	c_f	1497 m s^{-1}
Dynamic viscosity[a]	μ_f	0.891×10^{-3} Pa s
Bulk viscosity[b]	$\mu_b f$	2.47×10^{-10} Pa^{-1}
Compressibility	κ_f	448×10^{-12} Pa^{-1}
PDMS		
Density[c]	ρ_{PDMS}	920 kg m^{-3}
Speed of sound[d]	c_{PDMS}	1076.5 m s^{-1}
Pyrex		
Density[e]	ρ_{Pyrex}	2230 kg m^{-3}
Speed of sound[e]	c_{Pyrex}	6556.14 m s^{-1}
Lithium Niobate		
Density[f]	ρ_{LN}	4650 kg m^{-3}
Speed of sound[g]	c_{LN}	3994 m s^{-1}
Geometry		
Channel radius	r_{geo}	75 μm
Wavelength	λ	300 μm
Displacement amplitude	d	0.1 nm
Polystyrene		
Density[b]	ρ_{ps}	1050 kg m^{-3}
Speed of sound[g]	c_{ps}	2350 m s^{-1}
Compressibility[h]	κ_{ps}	249×10^{-12} Pa^{-1}
Case study		
Case 1		26.626 MHz
Case 2		53.253 MHz

[a][43], [b][44], [c][45], [d][46], [e][47], [f][48], [g][42], [h][49]

2.2 Material and properties

The purple perpendicular cross section is filled with water. Microchannel material is considered a rigid wall (Pyrex) and a soft wall (PDMS). Polystyrene particles are selected to show particle trajectories in the acoustophoretic section. The relevance properties of each domain and particle are listed in Table 1.

3 Governing equations

Nonlinear behavior of acoustic waves in fluid results in acoustic radiation forces [50] and drag force induced by acoustic streaming [51]. The interplay of these two forces on suspended particles triggers acoustic separation. The device's physics laws are the coupling of elastic, electrostatic, and fluid dynamic equations, which are computationally expensive to solve simultaneously. In this research, governing physics of full device is replaced with boundary conditions, and the proposed model is reduced to the fluid domain.

Governing equations of the fluid motion are the balance of conservation of mass and conservation of momentum. These equations with the equation of state give an well-posed set of governing equations of the physics [52].

$$\partial_t \rho = -\nabla \cdot (\rho v) \tag{1}$$

$$\rho \partial_t v + \rho(v \cdot \nabla)v = -\nabla p + \mu \nabla^2 v + \left(\mu_b + \frac{1}{3}\mu\right)\nabla(\nabla \cdot v) \tag{2}$$

$$p = c_0^2 \rho \tag{3}$$

where ρ is the fluid density, p is the fluid pressure, v is the fluid velocity, η is the fluid dynamic viscosity, β is the viscosity ratio defined as $(\mu_b/\mu + 1/3)$ and μ_b is the fluid bulk viscosity. In this research, because of the insignificant temperature variation, the energy equation is not solved. By employing Nyborg [53] perturbation technique, first- and second-order equations are derived.

$$v = v_0 + \varepsilon v_1 + \varepsilon^2 v_2 + O(\varepsilon^3) \tag{4}$$

$$p = p_0 + \varepsilon p_1 + \varepsilon^2 p_2 + O(\varepsilon^3) \tag{5}$$

$$\rho = \rho_0 + \varepsilon \rho_1 + \varepsilon^2 \rho_2 + O(\varepsilon^3) \tag{6}$$

Varepsilon, $0 < \varepsilon \ll 1$ is defined as the ratio of maximum SAW displacement of the substrate to the characteristic length [54]. Zero subscripts denote the quiescent state of the flow which in this research, the subscript indicates the fluid flow in the absence of acoustic field.

3.1 First order

Substituting zero- and first-order of Eqs. 4, 5 and 6 to the set of governing Eqs. 1 and 2, first order of equations reads:

$$\partial_t \rho_1 = -\rho_0 \nabla v_1 \tag{7}$$

$$\rho_0 \partial_t v_1 = -\nabla p_1 + \eta \nabla^2 v_1 + \beta \eta \nabla(\nabla \cdot v_1) \tag{8}$$

Equations 7 and 24 represent the governing equation for the acoustic field with viscosity and compressibility loss.

3.2 Second order

First-order results are time-dependant sinusoidally varying solutions to the acoustic field. Substituting second-order approximation of Eqs. 4, 5 and 6 to the set of governing Eqs. 1 and 2 gives governing equations of fluid flow in the presence of acoustic wave.

$$\langle \partial_t \rho_2 \rangle = -\rho_0 \nabla \cdot (\langle v_2 \rangle) - \nabla \cdot (\langle \rho_1 v_1 \rangle) \tag{9}$$

$$\rho_0 \langle \partial_t v_2 \rangle = -\nabla \langle p_2 \rangle - \eta \nabla^2 \langle v_2 \rangle + \beta \eta \nabla(\nabla \cdot \langle v_2 \rangle) \\ - \langle \rho_1 \partial_t v_1 \rangle - \rho_0 \langle (v_1 \cdot \nabla)v_1 \rangle \tag{10}$$

where $A(t)$ denotes time average of complex-valued field $A(t)$ with harmonic time-dependence $e^{-i\omega t}$ over a full oscillation period. For a product of two time-harmonic fields in the complex-valued field, the time average can be derived as $< A(t)B(t) >= \frac{1}{2}Re[A(0)^*B(0)]$, where the asterisk represents complex conjugation. Here, pressure and velocity with subscripts of two represent acoustic radiation pressure and acoustic streaming velocity, respectively.

3.3 Forces on particle

Forces acting on particles are acoustic radiation force due to scattering of the acoustic wave on particles, drag force induced by streaming velocity, gravity force, and buoyancy force. The Temperature variation is not significant, and its thermal effect is ignored. Equation of acoustic radiation force derived by [55] is taken into account. It is assumed that particle radius r is much smaller than the wavelength λ.

$$F^{rad} = -\pi r^3 \left[\frac{2}{3}\beta_f Re[f_1^* p_1^* \nabla p_1] - \rho_f Re[f_2^* v_1^* \cdot \nabla v_1]\right] \tag{11}$$

$$f_1 = 1 - \frac{\beta_p}{\beta_f} \tag{12}$$

$$f_2 = \frac{2(1-\gamma)(\rho_p - \rho_f)}{2\rho_p + \rho_f(1-3\gamma)} \tag{13}$$

$$\gamma = -\frac{3}{2}[1 + i(1 + \tilde{\delta})]\tilde{\delta} \tag{14}$$

$$\tilde{\delta} = \frac{\delta}{a} \tag{15}$$

$$\delta = \sqrt{\frac{2\mu}{\omega\rho_0}} \tag{16}$$

Where β_p is particle compressibility, β_f is fluid compressibility, ω is the angular velocity, δ is viscous boundary layer thickness, and the asterisk denotes the complex conjugate of the quantity. Drag force expression for spherical particles in a fluid is estimated as

$$F^{drag} = 6\pi\mu r(\langle v_2 \rangle - v_p) \tag{17}$$

The influence of gravity and buoyancy force is taken the form in Eq. 18:

$$F^{buoyancy} = \frac{4}{3}\pi r^3(\rho_f - \rho_{particle})g \tag{18}$$

Equations 11, 17, and 18 are exerted on particles to calculate particle trajectories.

4 Boundary conditions

Identification of exact relevance boundary conditions has been one of the challenging subject in acoustofluidic. The previous study reported appropriate boundary conditions to simulate SAW [32] in the microchannel with experimental validation. The bottom wall is excited by two incoming waves from IDT, which set up standing SAW (SSAW) in the channel. The operating frequencies in this study are assumed high enough to make smaller wavelengths than substrate thickness to prevent formation of any unwanted wave. As shown in Fig. 2, on the bottom horizontal boundary, Eqs. 19 and 20 as horizontal and vertical components, and on the circular boundary, Eq. 21 is imposed.

$$u_{x,pz} = 0.6u_0[e^{-C_d(w/2+x)}e^{i[2\pi(x-w/2)/\lambda-\omega t]}$$
$$+ e^{-C_d(w/2-x)}e^{i[2\pi(w/2-x)/\lambda-\omega t]} \tag{19}$$

$$u_{y,pz} = u_0[e^{-C_d(w/2+x)}e^{i[2\pi(x-w/2)/\lambda-\omega t+\pi/2]}$$
$$+ e^{-C_d(w/2-x)}e^{i[2\pi(w/2-x)/\lambda-\omega t+\frac{\pi}{2}+\pi]}] \tag{20}$$

Here, u_0 is displacement amplitude, w is microchannel width and C_d is decay coefficient. The C_d decay coefficient is expressed in Eq. 21 [56].

$$C_d = \frac{\rho_f c_f}{\rho_{LN} c_{LN}\lambda} \tag{21}$$

In the working frequency 13.313 MHz, C_d equals to $267.88\frac{1}{m}$. The wall behavior is replaced with impedance boundary condition, which acts as a resistant wall to the acoustic wave. This boundary condition acts as a rigid wall for hard material such as glass and as a lossy wall for soft material such as PDMS.

$$Z_w = \rho_w c_w \tag{22}$$

Combining first and second-order equations with explained boundary conditions makes the system fully determined. We employ zero-velocity (no-slip and solid-wall) boundary conditions at all walls for the time-averaged second-order equations, similar to those used in the previous study [17, 42].

5 Results and discussion

5.1 Grid study

The free triangular mesh is used in the domain to capture the governing physics in the microchannel correctly. Also, the coarse mesh elements are set up in the domain and progressively improve to find the best and optimized mesh to capture the exact first- and second-order values. Parameter MC is introduced as the number of mesh on the domain boundary to investigate its behavior on mesh convergence. The computational mesh is shown in Fig. 3. In line with the previous study, defined relative convergence parameter $C(g)$ by Muller is applied [17]. For each grid, convergence parameter $C(g)$ taken from in Eq. 23 is examined. $C(g)$ for a

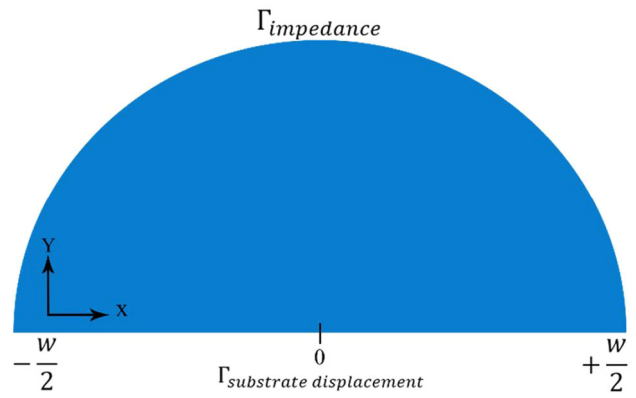**Fig. 2** Perpendicular two-dimensional cross section and imposed boundary condition

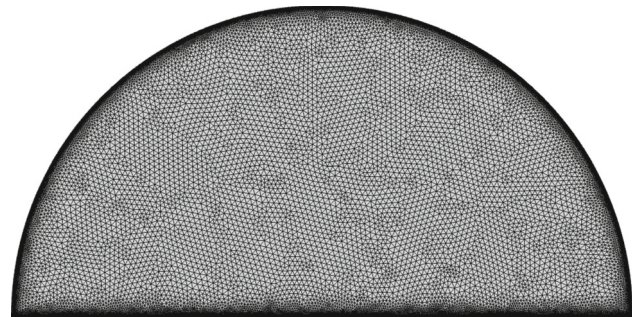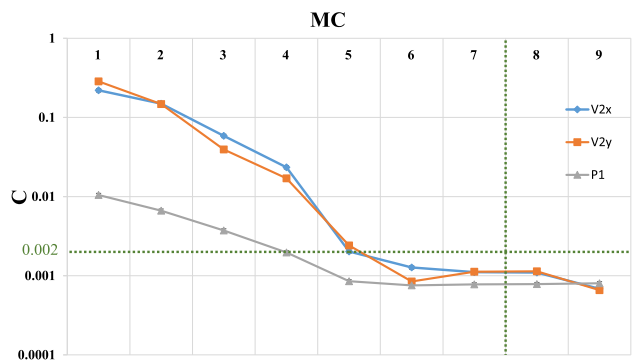**Fig. 3** Computational mesh

Fig. 4 Grid study

given field $g(x, y)$ is calculated where g_{ref} is taken from finer mesh value. For the selected Grid 8, illustrated in Fig. 4, $C(g)$ is less than 0.002, and parameters are calculated on this grid with 490 elements on the boundary.

$$C(g) = \sqrt{\frac{\int (g - g_{ref})^2 \mathrm{d}y\mathrm{d}x}{\int (g_{ref})^2 \mathrm{d}y\mathrm{d}x}} \tag{23}$$

5.2 Verification

We have calculated time-averaged second-order velocity in a rectangular channel with 600 µm width and 125 µm height to verify our numerical results. As depicted in Fig. 5, the time-averaged second-order velocity $\langle v_2 \rangle$ is calculated 1.76 µm/s in the strongest region, which is almost same value (1.72 µm/s) derived by Nama [42] in the same region. Comparing to Nama's research, there are four streaming vortices in the channel width, which near the bottom boundary, streaming power is considerably more significant than the bulk of the domain. No streaming rolls known as Schlichting streaming have been observed in the acoustic boundary layer too.

5.3 Frequency effect on acoustic fields and fluid flow

In this section, the behavior of acoustic fields is investigated. The acoustic pressure field and the acoustic velocity field for Pyrex wall are depicted in Fig. 6a, b, sequentially. The channel radius and the wavelengths are selected 75 µm and 300 µm, respectively, to match the half-wavelength in the channel width. This selection is widely applied in practical sorting application. As it is shown,
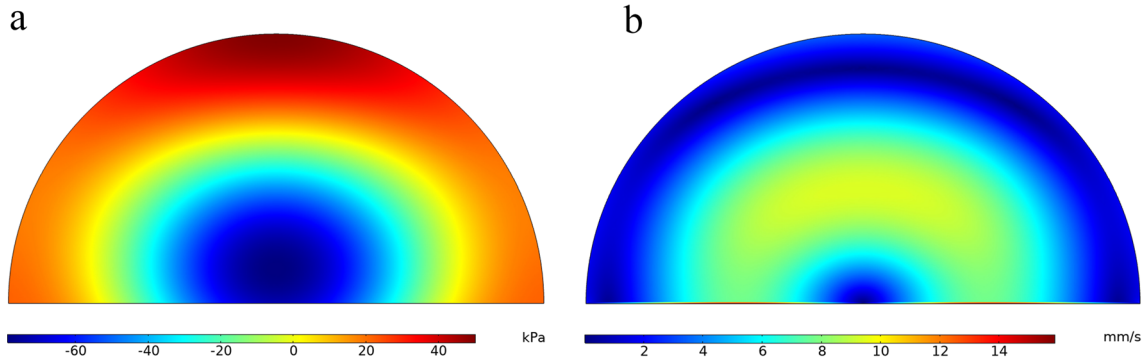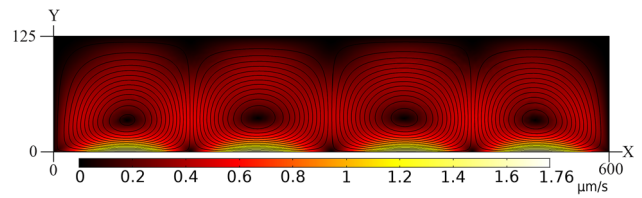
Fig. 5 Second-order
time-averaged velocity

Fig. 6 First-order acoustic fields. **a** Acoustic pressure field. **b** Acoustic velocity field for Pyrex
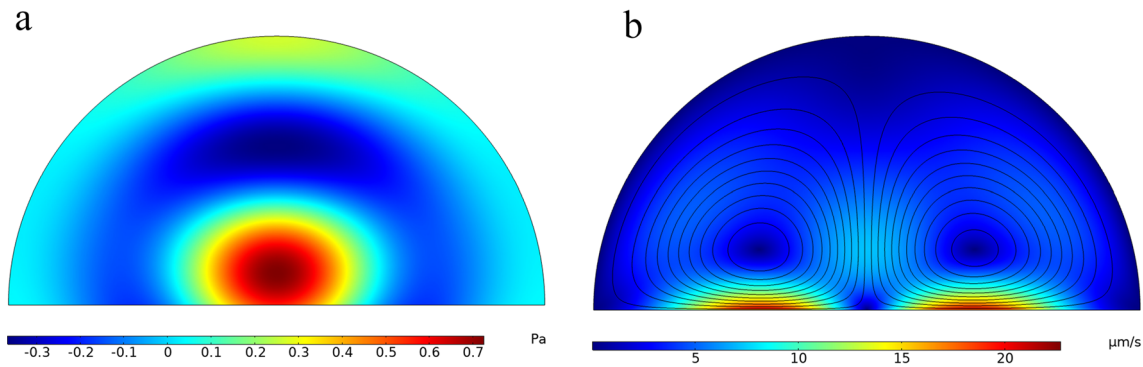

Fig. 7 a Time-averaged of second-order pressure, **b** Time-averaged second-order velocity

the pressure is varied from − 70.9 to 50.1 kPa (maximum pressure). The pressure node and anti-node are shaped circularly in the channel so that the pressure node is set up as a semi-circle with a smaller radius. The wall effect on the first-order acoustic field is reduced significantly. As shown in Fig. 6b, the acoustic velocity field is varied from zero at walls and the channel center to 15.9 mm/s as a maximum at the circular region. The acoustic velocity field is considerably changed by the traveling wave coming from the bottom to the top of the channel due to the aspect ratio of the channel (channel height is comparable to its width). The circular acoustic field shape arises from the uniform impedance of the wall.

Figure 7a shows the time-averaged second-order pressure. The pressure is shaped circularly, similar to the first-order fields. It is varied from −0.37 to 0.72 Pa. The high and low values are shown in the center of the channel. In Fig. 7b, acoustic steaming with the maximum value of 22.7 μm/s is depicted. Two streaming rolls with similar strengths are shaped in the channel width. Close to the vibrating wall, streaming velocity is much greater in value than the bulk velocity of the fluid. Despite the difference in the first-order pressure field between semicircular and rectangular microchannels [42], the acoustic streaming pattern is very similar in mentioned geometries. Streaming vortices follows the curvature of the channel and top region of the channel is weakly influenced by streaming presence.

In Fig. 8, pressure acoustic and time-averaged second-order velocity of two cases which is introduced in Table 1 is depicted. In both cases, the pressure node is set on the channel width. In the first case, acoustic pressure amplitude oscillates between −159 and +159 kPa, and time-averaged second-order velocity reaches 66.9 μm/s at maximum value. Acoustic pressure is stronger in the channel sides, and its strength decreases in the center, resulting in the rise in decay coefficient value. Four streaming rolls formed in the channel. Side rolls are stronger than center streaming rolls because of decay in the acoustic wave and diffractive effect. In the second case, the acoustic pressure field fluctuates between − 228 and + 228 kPa in an irregular pattern in both the width and height direction. Higher frequency makes the pressure anti-node regions smaller. This irregular pattern is not suitable for the acoustic sorting of particles. In this case, the pressure anti-node region closer to the channel side are stronger too. Toward the top of the channel, the traveling wave strength coming from bottom to top reduces. The acoustic streaming value rises to 118 μm/s at maximum value.
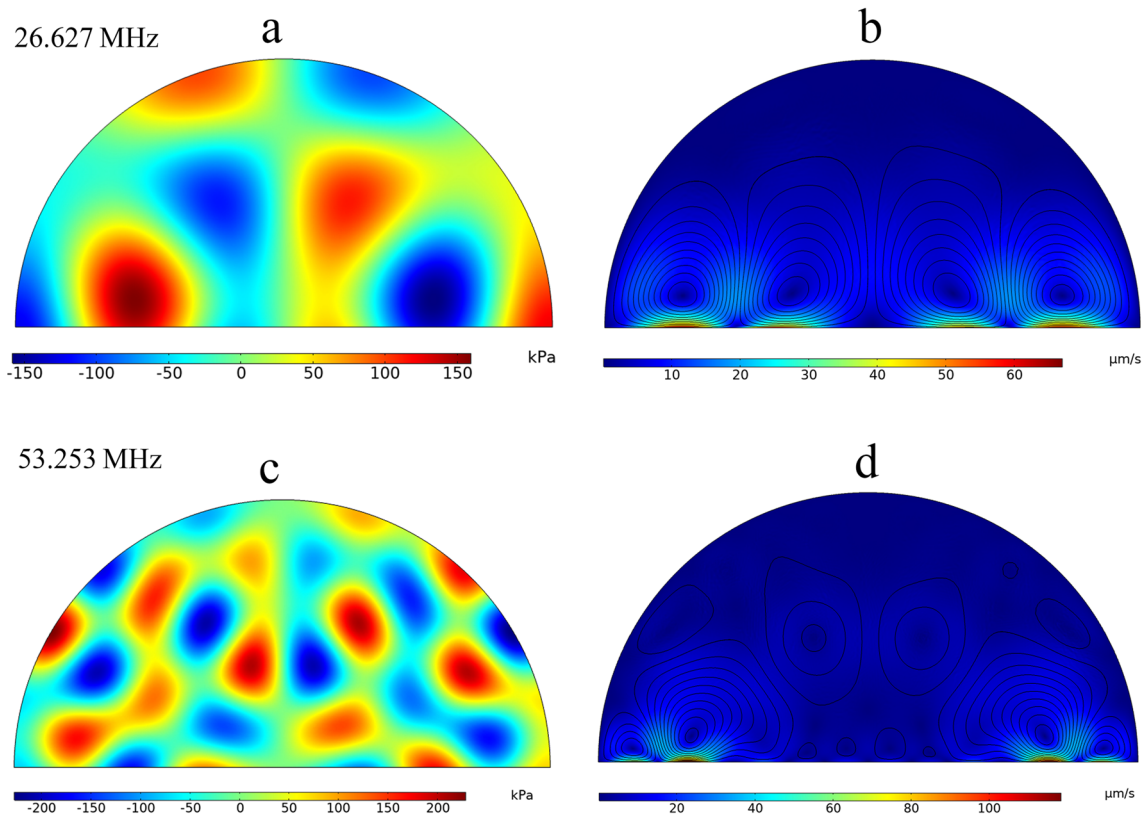
Fig. 8 a Acoustic pressure field in the frequency of 26.627 MHz, **b** Acoustic streaming in the frequency of 26.627 MHz, **c** Acoustic pressure field in the frequency of 53.253 MHz, **d** Acoustic streaming in the frequency of 53.253 MHz
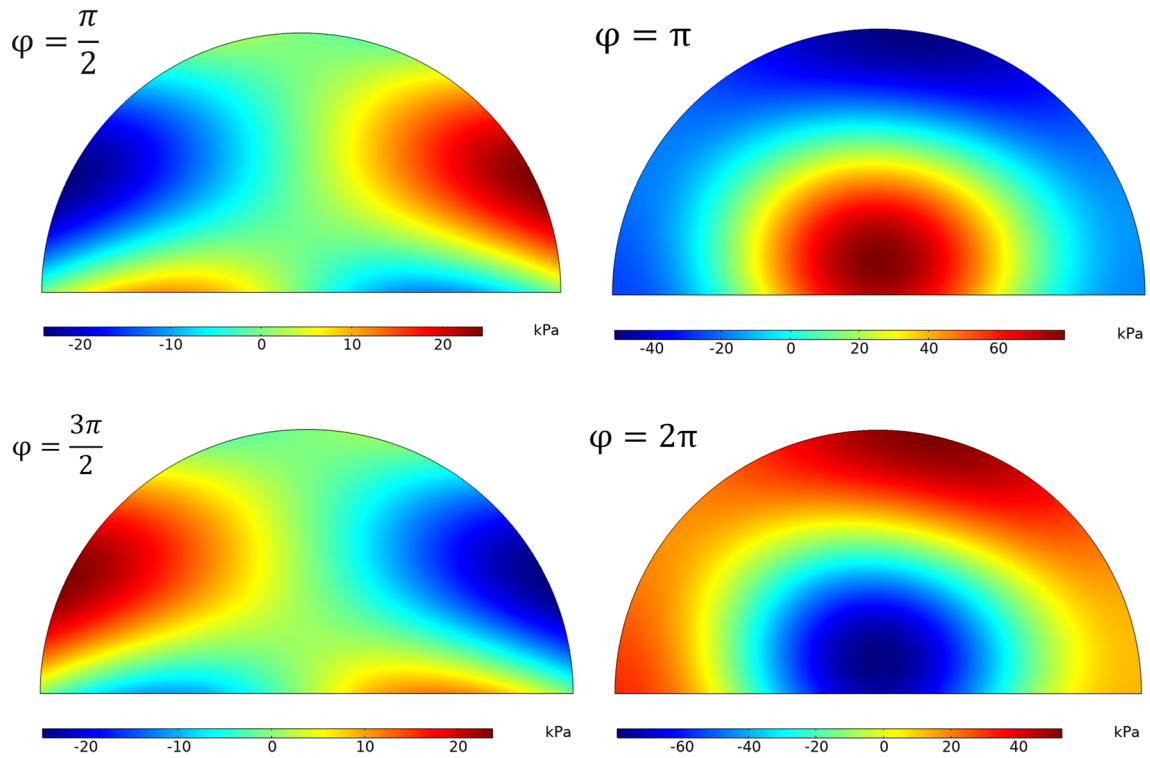

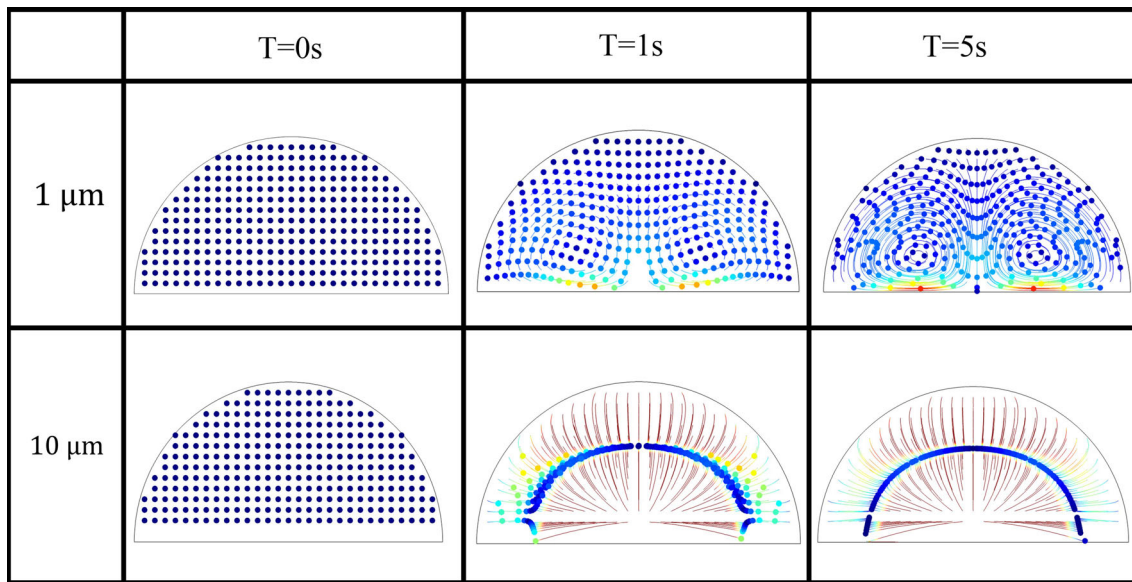**Fig. 9** Acoustic pressure field in different phase difference

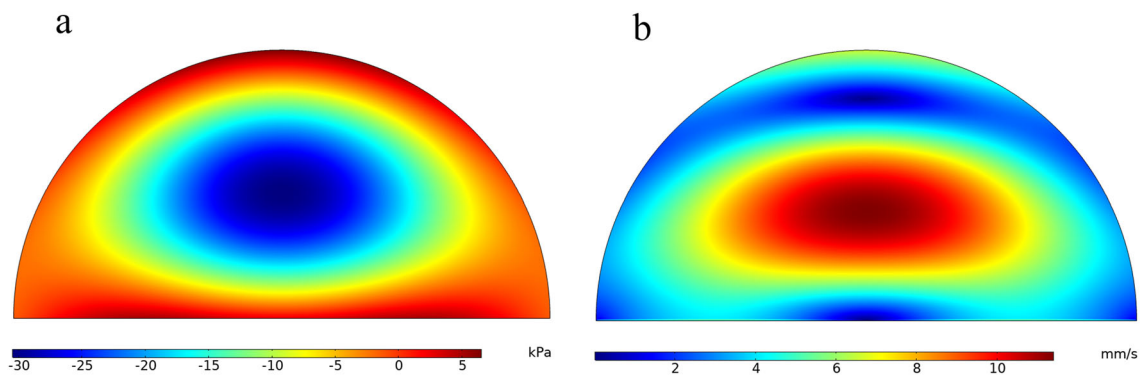**Fig. 10** Particle motion in different times

Fig. 11 PDMS wall. First-order acoustic fields. **a** Acoustic pressure field. **b** Acoustic velocity field
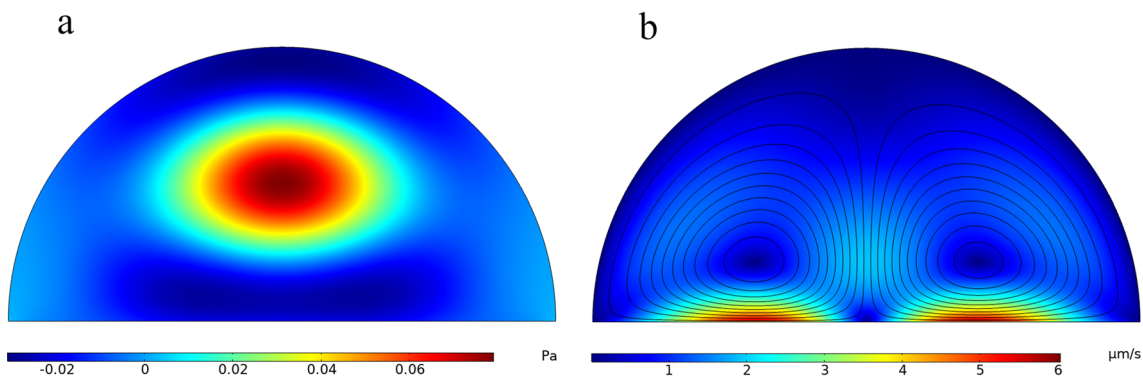

Fig. 12 PDMS wall. **a** Time-averaged second-order pressure, **b** time-averaged second-order velocity

Eight streaming rolls are shaped in the channel width which center rolls are weaker than the side rolls. Stronger sidewall vortices imply that in mixing application, sheath flow (streaming through sidewall region) benefit from perpendicular streaming to mix itself to the buffer flow (streaming through the center region). Even though the channel height is not too high, it is not entirely influenced by acoustic field, and the acoustic streaming value is close to zero at the top of the channel. Comparing acoustic streaming in cases one and two, it can be grasped that the standing wave creates four streaming rolls in the channel. Also, as it is shown, Frequency increase results in stronger acoustic field and acoustic streaming. Comparing Fig. 8b, c, by increasing the frequency, streaming rolls are split into smaller vortices but higher velocity.
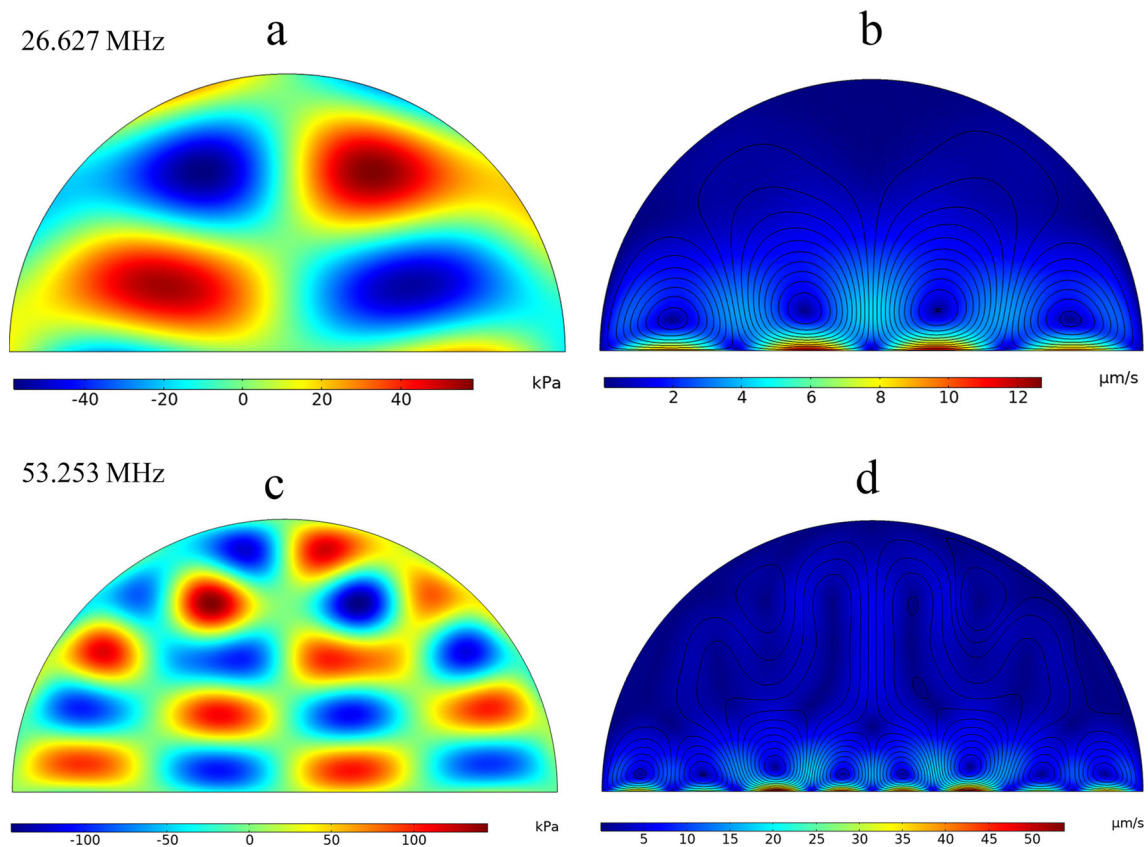
26.627 MHz

53.253 MHz

Fig. 13 First and second-order values for PDMS wall. **a** Acoustic pressure field in the frequency of 26.627 MHz, **b** Acoustic streaming in the frequency of 26.627 MHz, **c** Acoustic pressure field in the frequency of 53.253 MHz, **d** Acoustic streaming in the frequency of 53.253 MHz

Figure 9 displays the first-order acoustic pressure field in different phase values. By varying the phase difference, the amplitude and the pressure node and anti-node locations are changed. As it is shown, phase differences of $\frac{\pi}{2}$ and $\frac{3\pi}{2}$ are not appropriate for separation application since the pressure node is shaped both vertically and horizontally. In phase differences of π and 2π, the pressure node is shaped circularly, preparing a region to separate particles. The average pressure amplitude variation range for the phase differences of $\frac{\pi}{2}$ and $\frac{3\pi}{2}$ is proximately 48.35 kPa whereas this value for the phase difference of π and 2π is 133.5 kPa, more than two times greater in value than the last case. Contrary to the BAW systems, in which pressure anti-node can shape very well due to vibrating material in resonance mode, in SAW systems, selection of pressure anti-node on the wall does not result in the desired consequence.

5.4 Particle trajectories

The motion of polystyrene particles in two different diameters is studied. Half-wavelength is set up in the channel width, and the microchannel wall is Pyrex. The circularly shaped pressure node provides an appropriate pattern to separate particles. It is mentioned that polystyrene in water is attracted toward the pressure node due to the positive acoustic contrast factor. The motion of particles in two diameters of 1 μm and 10 μm is illustrated in Fig. 10. Particles with smaller sizes follow the acoustic streaming flow, while acoustic radiation force is dominant for more significant particles. The smaller particles, after 1 second, did not move sensibly while the larger particles are attracted to the pressure node. After five seconds, all larger particles are aggregated in the pressure node in the semicircular pattern, whereas the smaller particles could not follow the streaming patterns. These promising results represent that particles are not aggregated where acoustic streaming is dominant.

5.5 Wall effect on acoustic fields and fluid flow

In this section, the behavior of PDMS as a microchannel material is investigated. In Figs. 11a and 12a, first and second-order values are depicted, respectively. The acoustic pressure field is varied from −30.5 to 6.49 kPa (maximum value), and the first-order acoustic velocity is varied from zero to 11.4 mm/s. Figure 12b, Shows the acoustic streaming velocity. Streaming rolls generated in the channel are similar to the hard wall, and its value is 6.03 μm/s at maximum value. The critical difference between Pyrex and PDMS walls is the strength of the pressure field. Pyrex creates a more robust pressure field with the same excitation system,
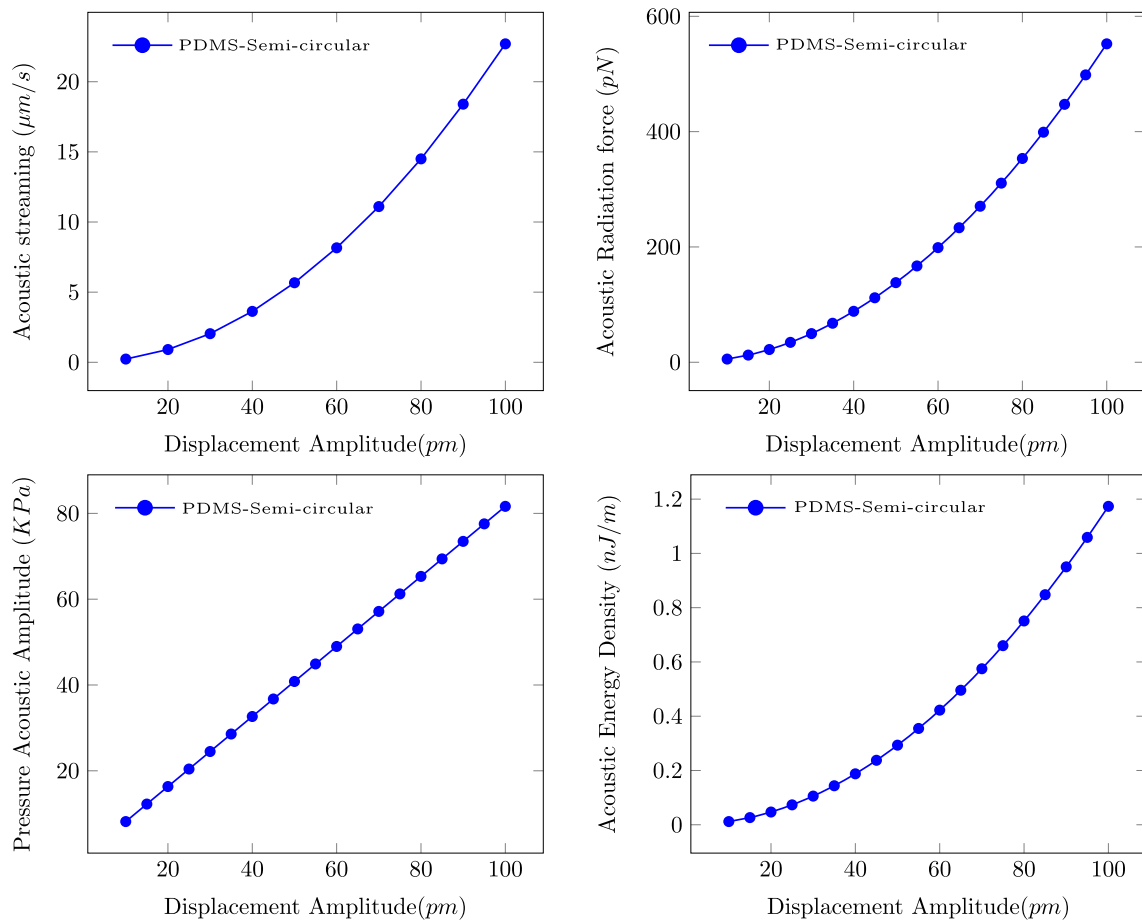
Fig. 14 Displacement amplitude effect on first-order and second-order values

which creates a stronger radiation force. When particle ACF and particle size are similar in applying acoustic particle separation, a stronger pressure field is necessary to change lateral displacement significantly. To augment the acoustic radiation force, increasing the frequency and displacement amplitude may be suggested. Nevertheless, frequency and voltage increment impose temperature gradients on the system, which is hazardous to biological cells. Time-averaged second-order acoustic pressure is varied from -0.03 to 40.08 Pa. Comparing PDMS first- and second-order pressure value to corresponding values of Pyrex, It is derived that energy loss in PDMS is remarkably more than Pyrex and the reflected wave from the rigid wall create a stronger acoustic field.

In this section, similar to the pervious section, cases one and two for PDMS walls are studied. In Fig. 13, first-order acoustic pressure and time-averaged second-order for two cases are illustrated. In the first case, the pressure node is shaped at the channel center, and two pressure anti-node are set up in the channel width with fluctuation amplitude of -58.2 kPa and $+58.2$ kPa. There are also two pressure anti-node set up in the channel height. In this case, acoustic streaming reaches $12.7\,\mu$m/s at the maximum value. There are four streaming rolls in the channel width. In contrast to Pyrex material, the streaming rolls affect the fluid close to the top wall. By increasing the frequency to the 53.253 MHz, the number of pressure anti-node regions increases and amplitude oscillates between -145 and $+145$ kPa and acoustic streaming increases to $53.7\,\mu$m/s. In contrast with Pyrex, PDMS prepare the appropriate region to sort particles in high frequencies. Similar to the first case, streaming rolls impact the bulk of fluid even close to the top wall. A crucial point in comparing results in different frequencies, both for PDMS and Pyrex wall, is a significant increase in the first-order acoustic fields and time-averaged second-order values by raising the frequency. For instance, comparing these two cases, the acoustic pressure amplitude of high frequency is nearly two times greater than lower frequency, and the time-averaged second-order velocity of higher frequency is nearly four times greater than lower frequency.

Fig. 15 Acoustic pressure field formed in different microchannel cross-section shape
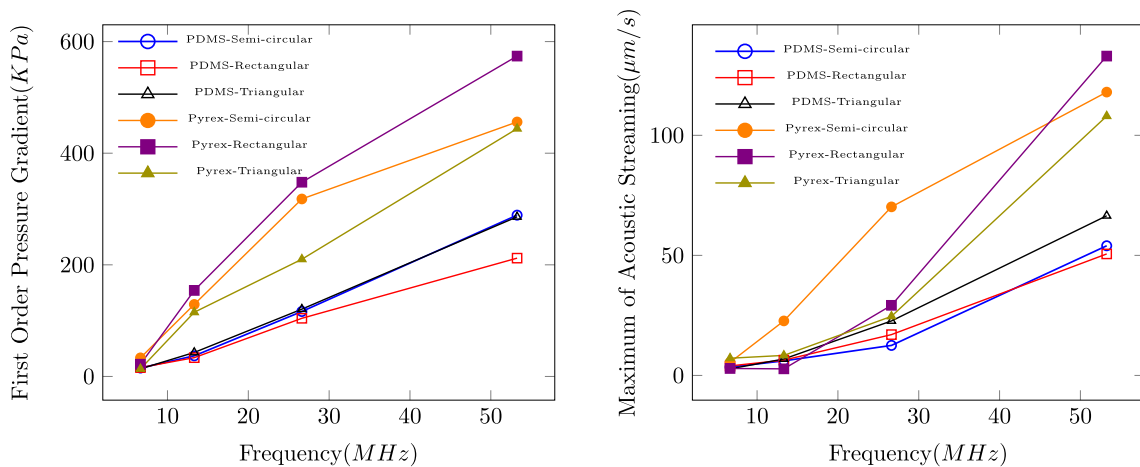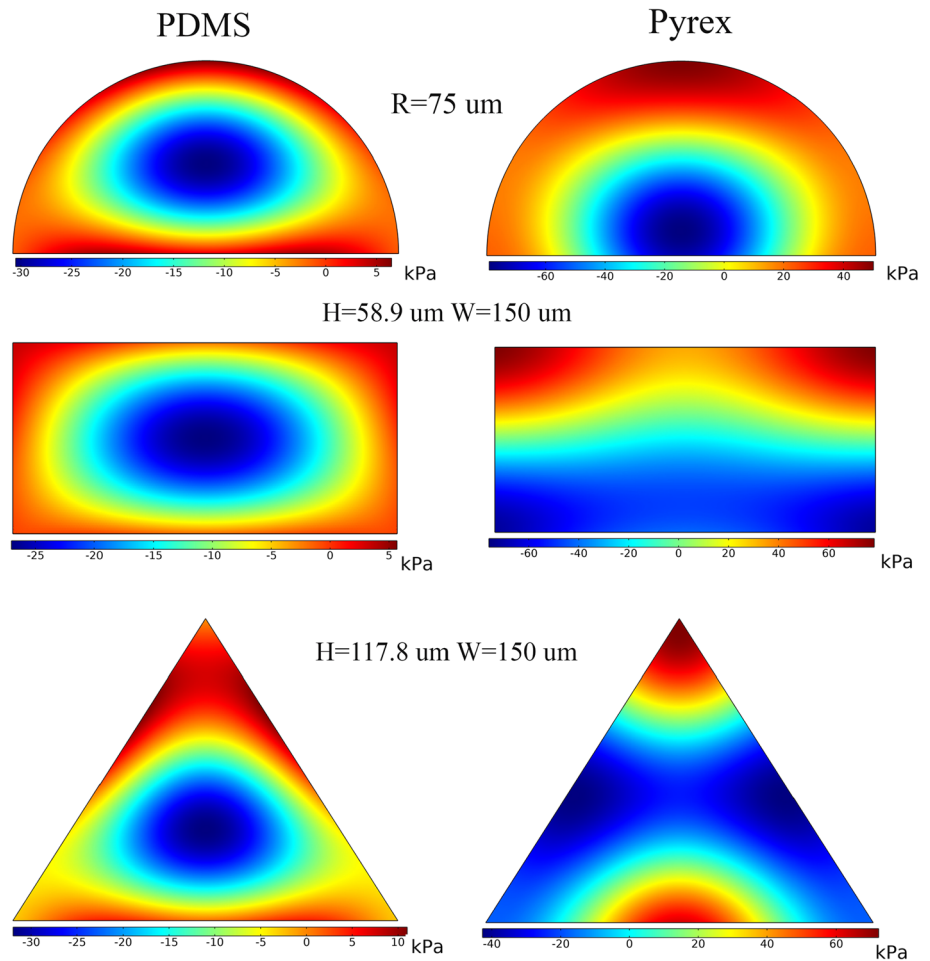

Fig. 16 Effect of the shape and frequency on acoustic pressure field and acoustic streaming

5.6 Displacement amplitude effect on acoustic fields and fluid flow

Displacement amplitude effect on first-order and second-order values as a representative of voltage variance is studied in this section. The time-averaged acoustic energy density E_{ac} in the fluid becomes [57]:

$$E_{ac} = \frac{1}{2}\kappa \langle p_{ac}^2 \rangle + \frac{1}{2}\rho \langle v_{ac}^2 \rangle \tag{24}$$

The acoustic energy density is integrated on area of the cross sections to include all the region.

In a comprehensive study, different displacement amplitudes ranging from 0.01 to 0.1 nm by step of 0.01 nm are studied. In Fig. 14, the maximum acoustic streaming velocity is depicted, which grows by the power of two. At displacement amplitude of 0.01 nm and 0.1 nm, acoustic streaming value is $0.23\,\mu$m/s and $22.7\,\mu$m/s, respectively. In Fig. 14, acoustic radiation force amplitude for polystyrene particles in different displacement amplitude is depicted. This graph grows as sharp as the acoustic streaming value. At displacement amplitude of 0.01 nm and 0.1 nm, the acoustic radiation force value is 5.5227 pN and 552.27 pN, respectively. In Fig. 14, Acoustic pressure amplitude for different displacement amplitude is depicted. The nonlinear growth behavior is seen in acoustic energy density variance while this growth for the pressure amplitude is linear. This study reveals that both nonlinear phenomena, including acoustic streaming, acoustic radiation, and acoustic energy density, have a quadratic dependency on displacement variation. Despite the nonlinear phenomena, acoustic pressure amplitude has a linear dependency on displacement variation. For acoustic separation applications, it is vital to know the growth rate of acoustic streaming. Another vital point to consider is, when particle sensibility to acoustic field presence is weak, dominant acoustic streaming can drastically reduce the recovery rate.

5.7 Effect of the cross-section shape

To explore the role of cross section of microchannel on the acoustic pressure field an acoustic streaming three different section is selected. Rectangular, triangular, and semi-circular sections are considered. At different working frequency for both PDMS and Pyrex material, the behavior of acoustic streaming and acoustic pressure is evaluated. Identical area and width are considered for meaningful comparison. Since, bottom width of the channel simulates acoustic wave behavior, width is similar in all cases. Figure 15 illustrates the acoustic pressure field at frequency of 13.313 MHz. For the PDMS wall, the shape of cross section does not influence the pressure field significantly. It is visible that the pressure-node and pressure anti-node in these cases are not suitable for particle sorting. The behavior of semi-circular, and rectangular sections is totally similar. Triangular shape enforce pressure nodes to be inclined near the wall. This design suggest for triangles with sharper angle ($H/W > 0.8$), the pressure node shaped in line region will be broken into different regions. Pyrex material response to cross-section changes is remarkable. Almost all cross sections create different pressure fields. All three shapes ca be applied to manipulate particles efficiently compared to the PDMS. Rectangular shape provide a uniform pressure node line and far away from the streaming regions. Figure 16, shows the acoustic streaming and acoustic pressure in different frequencies, material, and shapes. This figure helps to find a trade-off between AS and ARF. Acoustic pressure gradient and acoustic streaming for PDMS has less value magnitude comparing to Pyrex in all range of frequencies. The higher frequencies highlight more discrepancies between models. At frequency of 13.313 MHz, and 26.626 MHz, Pyrex semi-circular and triangle models with a low acoustic steaming magnitude provide a higher pressure gradient. PDMS-semi-circular model with less streaming value and higher pressure gradient is more efficient than other two PDMS models. It is also important to note, despite the higher streaming velocity of Pyrex semi-circular model, the pressure node is less influenced by the streaming roles due the existing distance. Assessment of the cross section clearly helps to find a trade-off between ARF and AS. It explicates the fact that for different application, different design is necessary and shapes of the channel play a key role.

6 Conclusion

The present numerical simulation successfully used a finite element scheme to model polystyrene beads motion in a semicircular microchannel filled with water and analyzing the critical operating parameters. The SAW microdevice is actuated by two counter-propagating surface acoustic waves that form a standing wave in the channel. Appropriate Boundary conditions from previous literature are used to capture the correct fluid behavior instead of the computationally expensive fully coupled system simulation.

This work investigates the acoustic field and laminar flow behavior surrounded by a rigid wall (Pyrex) and a soft wall (PDMS). To match half-, one and, two wavelengths in channel width, three different frequencies are studied. The importance of displacement amplitude on nonlinear acoustic phenomena and acoustic pressure amplitude is well investigated.

Comparison of different cross sections for Pyrex and PDMS material at different range of frequencies significantly help to find a trade-off between Acoustic Force(ARF) and AS. The key to finding is introducing different manipulation patterns for polystyrene particles without sensing the wall effect and acoustic streaming dominance. In each case study of frequency, device potential for sorting, separation, trapping, and mixing application is revealed. Investigating all effective operating parameters and comparing them with each other provides a powerful vision for the scientist to design an effective sorting device. Conventional and non-conventional cross section can provide efficient trapping region to sort particle with less streaming interference. The trade-off comparison and sensitivity analysis shows the great potential for enabling the improved design of acoustic separation application.

References

1. D.R. Reyes, D. Iossifidis, P.-A. Auroux, A. Manz, Micro total analysis systems. 1. Introduction, theory, and technology. Anal. Chem. **74**(12), 2623–2636 (2002)
2. P.-A. Auroux, D. Iossifidis, D.R. Reyes, A. Manz, Micro total analysis systems. 2. Analytical standard operations and applications. Anal. Chem. **74**(12), 2637–2652 (2002)
3. A. Farahinia, W. Zhang, I. Badea, Novel microfluidic approaches to circulating tumor cell separation and sorting of blood cells: a review. J. Sci. Adv. Mater. Device **6**, 303–320 (2021)
4. D.K. Deka, S. Pati, Influence of wettability and initial size on the merging dynamics of droplet within a y-shaped bifurcating channel. Fluid Dyn. Res. **53**, 035506 (2021)
5. C.W. Shields IV., C.D. Reyes, G.P. López, Microfluidic cell sorting: a review of the advances in the separation of cells from debulking to rare cell isolation. Lab Chip **15**(5), 1230–1249 (2015)
6. X. Bai, B. Song, Z. Chen, W. Zhang, D. Chen, Y. Dai, S. Liang, D. Zhang, Z. Zhao, L. Feng, Postoperative evaluation of tumours based on label-free acoustic separation of circulating tumour cells by microstreaming. Lab Chip **21**(14), 2721–2729 (2021)
7. A. Neild, S. Oberti, F. Beyeler, J. Dual, B.J. Nelson, A micro-particle positioning technique combining an ultrasonic manipulator and a microgripper. J. Micromech. Microeng. **16**(8), 1562 (2006)
8. A. Wixforth, C. Strobl, C. Gauer, A. Toegl, J. Scriba, Zv. Guttenberg, Acoustic manipulation of small droplets. Anal. Bioanal. Chem. **379**(7), 982–991 (2004)
9. L.Y. Yeo, J.R. Friend, Surface acoustic wave microfluidics. Annu. Rev. Fluid Mech. **46**, 379–406 (2014)
10. A. Urbansky, F. Olm, S. Scheding, T. Laurell, A. Lenshof, Label-free separation of leukocyte subpopulations using high throughput multiplex acoustophoresis. Lab Chip **19**(8), 1406–1416 (2019)
11. P. Augustsson, C. Magnusson, M. Nordin, H. Lilja, T. Laurell, Microfluidic, label-free enrichment of prostate cancer cells in blood based on acoustophoresis. Anal. Chem. **84**(18), 7954–7962 (2012)
12. A. Nilsson, F. Petersson, H. Jönsson, T. Laurell, Acoustic control of suspended particles in micro fluidic chips. Lab Chip **4**(2), 131–135 (2004)
13. X. Ding, Z. Peng, S.-C.S. Lin, M. Geri, S. Li, P. Li, Y. Chen, M. Dao, S. Suresh, T.J. Huang, Cell separation using tilted-angle standing surface acoustic waves. Proc. Natl. Acad. Sci. **111**(36), 12992–12997 (2014)
14. M. Wu, C. Chen, Z. Wang, H. Bachman, Y. Ouyang, P.-H. Huang, Y. Sadovsky, T.J. Huang, Separating extracellular vesicles and lipoproteins via acoustofluidics. Lab Chip **19**(7), 1174–1182 (2019)
15. M. Wu, P.-H. Huang, R. Zhang, Z. Mao, C. Chen, G. Kemeny, P. Li, A.V. Lee, R. Gyanchandani, A.J. Armstrong et al., Circulating tumor cell phenotyping via high-throughput acoustic separation. Small **14**(32), 1801131 (2018)
16. A. Shams Taleghani, M. Sheikholeslam Noori, Numerical investigation of coalescence phenomena, affected by surface acoustic waves. Eur. Phys. J. Plus **137**(8), 975 (2022)
17. P.B. Muller, R. Barnkob, M.J.H. Jensen, H. Bruus, A numerical study of microparticle acoustophoresis driven by acoustic radiation forces and streaming-induced drag forces. Lab Chip **12**(22), 4617–4627 (2012)
18. J. Lei, M. Hill, P. Glynne-Jones, Numerical simulation of 3d boundary-driven acoustic streaming in microfluidic devices. Lab Chip **14**(3), 532–541 (2014)
19. S. Liu, Y. Yang, Z. Ni, X. Guo, L. Luo, J. Tu, D. Zhang et al., Investigation into the effect of acoustic radiation force and acoustic streaming on particle patterning in acoustic standing wave fields. Sensors **17**(7), 1664 (2017)
20. P.B. Muller, H. Bruus, Numerical study of thermoviscous effects in ultrasound-induced acoustic streaming in microchannels. Phys. Rev. E **90**(4), 043016 (2014)
21. A. Tahmasebipour, L. Friedrich, M. Begley, H. Bruus, C. Meinhart, Toward optimal acoustophoretic microparticle manipulation by exploiting asymmetry. J. Acoust. Soc. Am. **148**(1), 359–373 (2020)
22. B.G. Winckelmann, H. Bruus, Theory and simulation of electroosmotic suppression of acoustic streaming. J. Acoust. Soc. Am. **149**(6), 3917–3928 (2021)
23. J.S. Bach, H. Bruus, Suppression of acoustic streaming in shape-optimized channels. Phys. Rev. Lett. **124**(21), 214501 (2020)
24. J. Lei, F. Cheng, K. Li, Z. Guo, Two-dimensional concentration of microparticles using bulk acousto-microfluidics. Appl. Phys. Lett. **116**(3), 033104 (2020)
25. J. Lei, F. Cheng, K. Li, Numerical simulation of boundary-driven acoustic streaming in microfluidic channels with circular cross-sections. Micromachines **11**(3), 240 (2020)
26. D.J. Collins, R. O'Rorke, C. Devendran, Z. Ma, J. Han, A. Neild, Y. Ai, Self-aligned acoustofluidic particle focusing and patterning in microfluidic channels from channel-based acoustic waveguides. Phys. Rev. Lett. **120**(7), 074502 (2018)
27. C. Devendran, T. Albrecht, J. Brenker, T. Alan, A. Neild, The importance of travelling wave components in standing surface acoustic wave (ssaw) systems. Lab Chip **16**(19), 3756–3766 (2016)
28. M.R. Dezfuli, A. Shahidian, M. Ghassemi, Quantitative assessment of parallel acoustofluidic device. J. Acoust. Soc. Am. **150**(1), 233–240 (2021)
29. N.R. Skov, P. Sehgal, B.J. Kirby, H. Bruus, Three-dimensional numerical modeling of surface-acoustic-wave devices: acoustophoresis of micro-and nanoparticles including streaming. Phys. Rev. Appl. **12**(4), 044028 (2019)
30. J.-C. Hsu, C.-L. Chao, Full-wave modeling of micro-acoustofluidic devices driven by standing surface acoustic waves for microparticle acoustophoresis. J. Appl. Phys. **128**(12), 124502 (2020)
31. Y. Zhou, Comparison of numerical models for bulk and surface acoustic wave-induced acoustophoresis in a microchannel. Eur. Phys. J. Plus **135**(9), 696 (2020)
32. R. Barnkob, N. Nama, L. Ren, T.J. Huang, F. Costanzo, C.J. Kähler, Acoustically driven fluid and particle motion in confined and leaky systems. Phys. Rev. Appl. **9**(1), 014027 (2018)
33. A. Vargas-Jiménez, M. Camacho, J. Muñoz, I. González, A 3d analysis of the acoustic radiation force in microfluidic channel with rectangular geometry. Wave Motion **101**, 102701 (2021)
34. C. Sun, F. Wu, Y. Fu, D.J. Wallis, R. Mikhaylov, F. Yuan, D. Liang, Z. Xie, H. Wang, R. Tao et al., Thin film gallium nitride (gan) based acoustofluidic tweezer: modelling and microparticle manipulation. Ultrasonics **108**, 106202 (2020)
35. E. Los Reyes, V. Acosta, P. Carreras, A. Pinto, I. González, Three-dimensional numerical analysis as a tool for optimization of acoustophoretic separation in polymeric chips. J. Acoust. Soc. Am. **150**(1), 646–656 (2021)
36. R.P. Moiseyenko, H. Bruus, Whole-system ultrasound resonances as the basis for acoustophoresis in all-polymer microfluidic devices. Phys. Rev. Appl. **11**(1), 014014 (2019)

37. W.N. Bodé, L. Jiang, T. Laurell, H. Bruus, Microparticle acoustophoresis in aluminum-based acoustofluidic devices with pdms covers. Micromachines **11**(3), 292 (2020)
38. C. Devendran, D.J. Collins, A. Neild, The role of channel height and actuation method on particle manipulation in surface acoustic wave (saw)-driven microfluidic devices. Microfluid. Nanofluid. **26**(2), 9 (2022)
39. X. Liu, X. Chen, Z. Yang, H. Xia, C. Zhang, X. Wei, Surface acoustic wave based microfluidic devices for biological applications. Sensors Diagnost. **2**, 507–528 (2023)
40. M. Ali, J. Park, Ultrasonic surface acoustic wave-assisted separation of microscale droplets with varying acoustic impedance. Ultrason. Sonochem. **93**, 106305 (2023)
41. G. Liu, W. Shen, Y. Li, H. Zhao, X. Li, C. Wang, F. He, Continuous separation of particles with different densities based on standing surface acoustic waves. Sens. Actuat. A **341**, 113589 (2022)
42. N. Nama, R. Barnkob, Z. Mao, C.J. Kähler, F. Costanzo, T.J. Huang, Numerical study of acoustophoretic motion of particles in a PDMS microchannel driven by surface acoustic waves. Lab Chip **15**(12), 2700–2709 (2015)
43. Y.A. Cengel, M.A. Boles, M. Kanoglu, *Thermodynamics: An Engineering Approach*, vol. 5 (McGraw-Hill, New York, 2011)
44. W.M. Haynes, *CRC Handbook of Chemistry and Physics* (CRC Press, Hoboken, 2014)
45. D. Armani, C. Liu, N. Aluru, Re-configurable fluid circuits by pdms elastomer micromachining. In: Technical Digest. IEEE International MEMS 99 Conference. Twelfth IEEE International Conference on Micro Electro Mechanical Systems (Cat. No. 99CH36291), pp. 222–227 (1999). IEEE
46. J.K. Tsou, J. Liu, A.I. Barakat, M.F. Insana, Role of ultrasonic shear rate estimation errors in assessing inflammatory response and vascular risk. Ultrasound Med. Biol. **34**(6), 963–972 (2008)
47. N.R. Skov, H. Bruus, Modeling of microdevices for saw-based acoustophoresis-a study of boundary conditions. Micromachines **7**(10), 182 (2016)
48. K.-K. Wong, Properties of Lithium Niobate vol. 28. IET (2002)
49. P.H. Mott, J.R. Dorgan, C. Roland, The bulk modulus and poisson's ratio of "incompressible" materials. J. Sound Vib. **312**(4–5), 572–575 (2008)
50. H. Bruus, Acoustofluidics 7: the acoustic radiation force on small particles. Lab Chip **12**(6), 1014–1021 (2012)
51. M. Wiklund, R. Green, M. Ohlin, Acoustofluidics 14: applications of acoustic streaming in microfluidic devices. Lab Chip **12**(14), 2438–2451 (2012)
52. H. Bruus, *Theoretical Microfluidics*, vol. 18 (Oxford University Press, Oxford, 2008)
53. W.L. Nyborg, Acoustic streaming due to attenuated plane waves. J. Acoust. Soc. Am. **25**(1), 68–75 (1953)
54. D. Köster, Numerical simulation of acoustic streaming on surface acoustic wave-driven biochips. SIAM J. Sci. Comput. **29**(6), 2352–2380 (2007)
55. M. Settnes, H. Bruus, Forces acting on a small particle in an acoustical field in a viscous fluid. Phys. Rev. E **85**(1), 016327 (2012)
56. J. David, N. Cheeke, Fundamentals and applications of ultrasonic waves (2017)
57. S. Sachs, M. Baloochi, C. Cierpka, J. König, On the acoustically induced fluid flow in particle separation systems employing standing surface acoustic waves-part I. Lab Chip **22**(10), 2011–2027 (2022)